

Implementation of the Bidirectional Reflectance Function for Modeling the Spectra Derived from Hyperspectral Images



R. Mohammed Zeeshan and B. Sayyad Shafiyoddin

Abstract Hapke's bidirectional reflectance function based on the theory of radiative transfer has been implemented for modeling the spectra derived from Chandrayaan-1 hyperspectral images. The parameter study was done to study the behavior and influence of each parameter like grain size, porosity, iron fraction which represents the degree of space weathering and phase function was critically assessed. The model was then tested against the four standard lunar mixtures which constitutes of major lunar minerals from RELAB, and it was observed that the artificially created model spectra were successful in reproducing the overall trend in the resultant spectra. Finally, the nine representative spectra derived from hyperspectral image of the Chandrayaan-1 HySI sensor covering part of Mare Vaporum were modeled. The mass fraction of the surface minerals along with the associated Hapke parameter was predicted.

Keywords Bidirectional reflectance · Hyperspectral image · Porosity

1 Introduction

The systematic effect of the space weathering process impedes our ability to study and interpret the meaning full information from the remotely acquired satellite images from the airless body like moon. The long-term exposure of the lunar surface accumulates significant amount of sub-microscopic iron in the first few millimeters of the lunar crust [1–6]. The laboratory studies from the lunar returns sample clearly show the difference between the spectra from the sensor measured images and the spectra from the laboratory samples having higher reflectance, strong absorption strength as compared to the spectra derived from the images [7–9]. The effect on the lunar soil spectra is reduction in overall reflectance, reddened-slope continuum and attenuated absorption bands. The above-given characteristics of the lunar spectra are due to long-time exposure to the harsh environment which forms a thin layer of the sub-microscopic iron (SMFe) on the lunar soil [10]. The micrometeorite bombardment

R. Mohammed Zeeshan · B. Sayyad Shafiyoddin (✉)
Department of Computer Science, Milliyya Arts, Science & Management Science College, Beed,
MS 431122, India

and the high-energy solar wind ion implantation are considered the two primary processes involved in space weathering [11–14]. When the high-energy solar wind ions strike on the lunar, soil causes sputtering of the iron particles from its lattice sites in adjacent soil grains and this sputtered iron particle ejects from soil surface as a single, uncharged atom, and redeposit on the surface of adjacent soil grains. The micrometeorite bombardment causes the target to partially vaporize and the meteorite fully vaporized and deposited on the soil, forming a thin layer on the crust containing high amount of iron. This thin layer of sub-microscopic iron complicates the spectral analysis from the imagery data. Figure 1 shows the workflow of the modeling process.

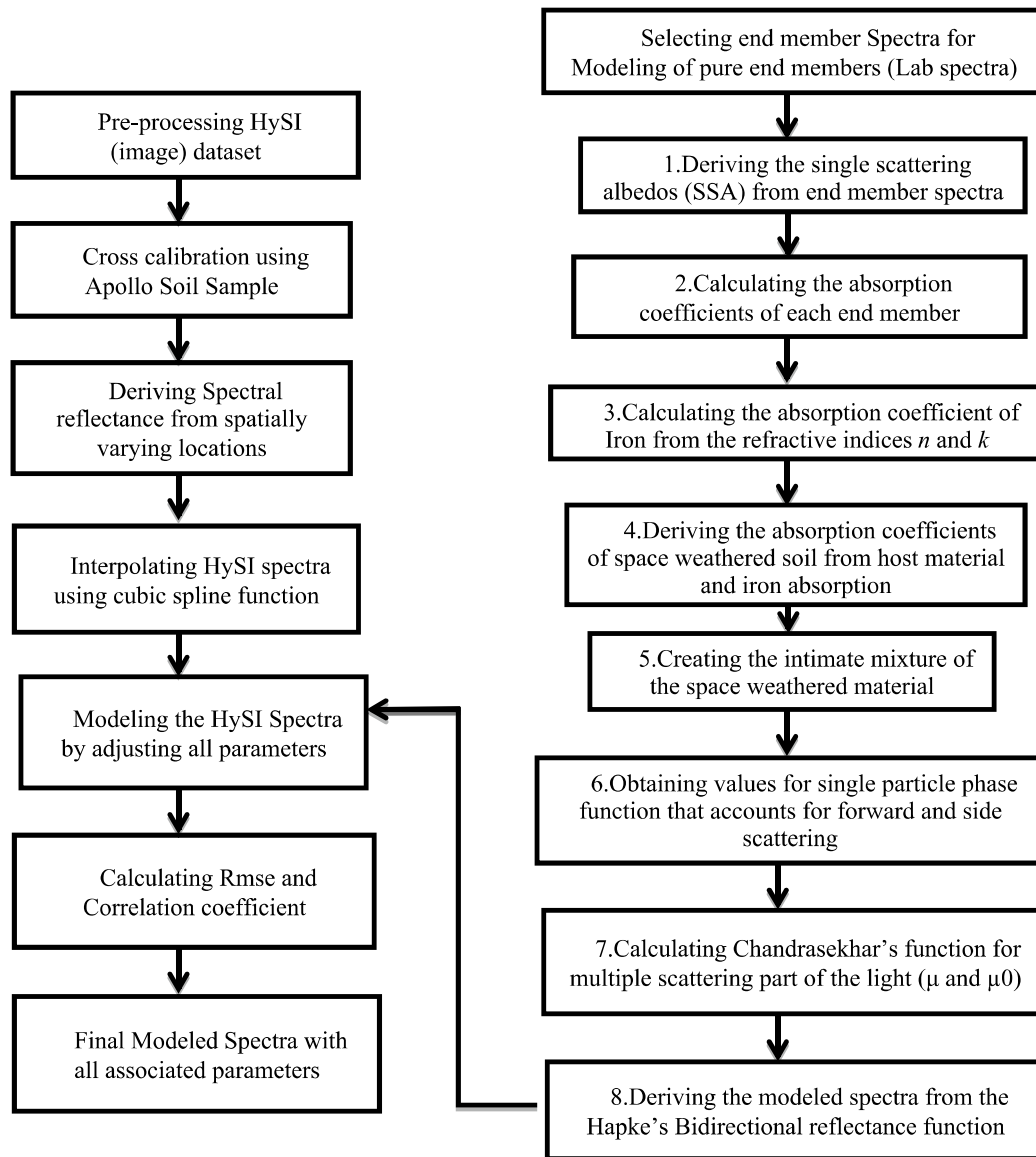


Fig. 1 Typical workflow for creating artificial spectra and modeling with the measured HySI image spectra

2 Literature Review

The Hapke's bi-directional reflectance equation based on the fundamental equation of radiative transfer that estimates the behavior of the electromagnetic waves when they interact with a particular medium. Three models are available that are commonly used to model the spectra derived from the airless bodies like moon; they are the Shkuratov model [15], Hapke's bidirectional reflectance function [16], and modified Gaussian model used by sunshine [17]. Each model has certain constraints like the Shkuratov model does not consider the role of viewing geometry means how the reflectance from a surface varies with the varying viewing geometry [15, 18]. Whereas the Hapke's model which assumes that the host material is an intimate mixture with particle size larger than the wavelength [19–23] and the modified Gaussian model employed to model the width, strength and band center of the absorption bands. In the presented work, we have implemented the Hapke model that easily accommodates the viewing geometry and other parameters widely used to model hence quantify the remotely acquired spectra [24–29]. Luceyin [26] has used the Hapke model to map the common major lunar minerals like plagioclase, olivine, clinopyroxene, and Orthopyroxene from relatively fresh areas. To model the measured reflectance spectra of Chandrayaan-1 hyperspectral imager (HySI), we have obtained an artificial reflectance spectrum using bidirectional reflectance function (BRDF) based on the equation of radiative transfer proposed by Bruce Hapke and published in the series of papers.

2.1 Model Definition and Implementation

Bidirectional reflectance function (BRDF) based on the equation of radiative transfer proposed by Bruce Hapke and published in the series of papers [19–23]. The bidirectional reflection function of a surface is given by Eq. (1).

$$r_B = K \frac{w}{4\pi} \frac{\mu_0}{\mu_0 + \mu} (1 + B(g)P(g) + H(\mu_0)H(\mu) - 1) \quad (1)$$

g denotes phase angle, and $P(g)$ is phase function defines the angular scattering pattern of particles in case of non-isotropic scattering, and it is 1 for isotropic scattering particles. $B(g)$ is opposition effect which is the unusual brightening with small phase angles due to shadow hiding where less shadows from upper grains on lower grains are visible and Chandrasekhar's H function is for multiple scattering part of the light. The main objective of the work is to model the HySI spectra using Eq. (1). For better prediction of the surface mineralogy with mass fraction along with the other parameters like grain size, porosity, phase function, degree of space weathering from the area under study by creating artificial reflectance spectra using pure end member spectra from RELAB and the analog artificial spectra is tested against the mixtures of the known composition.

The single-scattering albedo from a relationship exists between scattering efficiency and absorption coefficient given by Hapke [19] from which SSA was derived as shown in Eq. (2) from [23].

$$Q_S = w = (1 + \alpha D_e)^{-1} \quad (2)$$

where

$$D_e = \frac{2}{3} \frac{1 - S_E}{1 - S_I} D$$

The D_e is the particle diameter, and D is the mean photon path length. The S_E is the Fresnel reflection coefficient of the external light reflected by the particle, and S_I is the Fresnel reflection coefficient of the internal scattered light and defined by Eqs. (3) and (4), where n is the refractive index of each end member and calculated at each wavelength $n(\lambda)$. For plagioclase, pyroxene, and olivine, the refractive index from [30], and for the agglutinates, a refractive index for glass from [31] is assumed to be constant over our measured wavelength range.

$$S_E = \frac{(n - 1)^2}{(n + 1)^2} + 0.05 \quad (3)$$

and

$$S_I = 1 - \frac{4}{n(n + 1)^2} \quad (4)$$

The absorption coefficient from the equation is given in Eq. (5) for deriving alpha from Hapke paper [19].

$$\alpha = \frac{1}{D} \ln \left[S_I + \frac{(1 - S_E)(1 - S_I)}{w - S_E} \right] \quad (5)$$

We have calculated the absorption coefficient using the equation from the paper. The optical constants for iron n real part and k imaginary part were used from [32]. The absorption coefficient of iron can be derived using Eq. (6) where ϕ is the iron fraction and z is given by Eq. (7).

$$\alpha_{\text{Fe}} = \frac{36\pi}{\lambda} \phi z \quad (6)$$

where

$$z = \frac{n_h^3 n_{\text{Fe}} k_{\text{Fe}}}{(n_{\text{Fe}}^2 - k_{\text{Fe}}^2 + 2n_h^2)^2 + (2n_{\text{Fe}} k_{\text{Fe}})^2} \quad (7)$$

where n_h is the real part of the refractive index of pure end member, n_{Fe} is real part of the refractive index of iron, and k_{Fe} is the imaginary part of the refractive index of iron.

To add the effect of space weathering, the absorption coefficient of the host material has been derived from single scattering albedo (w) using Eq. (6). Here at this step, we have derived the absorption coefficient of space weathered material given by Eq. (8) by adding absorption coefficient of host material and the absorption coefficient of iron.

$$\alpha_{sw} = \alpha_{hm} + \alpha_{Fe} \quad (8)$$

From the absorption coefficient of space weathered material, we have derived the single scattering albedo w_{sw} of the space weathered material.

$$w_{sw} = (1 - \alpha_{sw} D_e)^{-1} \quad (9)$$

From Eq. (9), the SSA was obtained. After calculating the single scattering albedo, the intimate mixture was created.

To create the intimate mixture following Eq. (10) is used from B. Hapke's paper [16].

$$w_{im} = \sum_{i=1}^n \frac{M(i)}{\rho(i)d(i)} w_{sw}(i) \bigg/ \sum_{i=1}^n \frac{M(i)}{\rho(i)d(i)} \quad (10)$$

where M is the mass fraction, ρ is the single-particle density, and d is the average effective particle diameter.

The single-particle phase function for non-isotropic particles that scatters the light in varying angular patterns in all directions is known as non-isotropic scatterers. For mineral end members, this needs to be considered and can be finding out using two-term Legendre polynomials from Eq. (11) given in [33].

$$P(g) = 1 + b \cos(g) + c(1.5 \cos^2(g) - 0.5) \quad (11)$$

The porosity parameter K approximated by the following formula given by Eq. (12) and the value of parameter K varies between 1 and 6.

$$K = \frac{-\ln(1 - 1.209\emptyset^{1/3})}{1.209\emptyset^{1/3}} \quad (12)$$

The porosity parameter is connected via $P = 1 - \emptyset$ where \emptyset is the filling factor; as filling factor increases, the porosity decreases, and as porosity decreases, the reflectance increases. For very small filling factors, the porosity parameter becomes 1. Chandrasekhar's H function accounts for the multiple scattering part of the incoming light. The New approximation for Chandrasekhar's isotropic H function given in [34],

in this approximation, porosity is not included hence it can be only used without porosity and derived using Eq. (13).

$$H(x) = \frac{1 + \frac{2x}{K}}{1 + \frac{2\gamma x}{K}} \quad (13)$$

with

$$\gamma = \sqrt{1 - w} \text{ and } x = [\mu_0, \mu].$$

3 Parameter Study

The effect of each parameter on the spectral reflectance is studied in the following section.

3.1 Effect of Different Mineral Mass Fractions

The five pure end member selected from RELAB database are orthopyroxene, clinopyroxene, olivine, plagioclase, and agglutinates. The pure mineral mass fraction and by keeping 20% mass fraction of each end member can be seen in Fig. 2. The wavelength is clipped to 960 μm as of HySI spectral range. The complete spectral absorption for orthopyroxene around 900 μm can be seen, whereas the absorption for other end members is going beyond 964 μm .

Fig. 2 Effect of mineral mass fraction

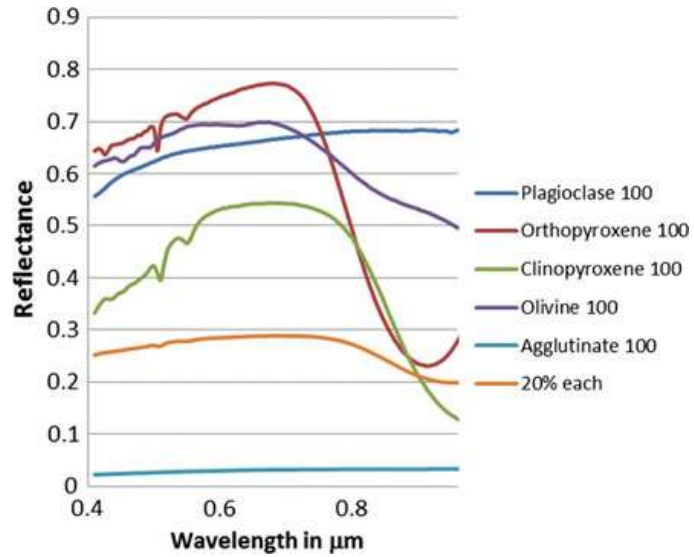
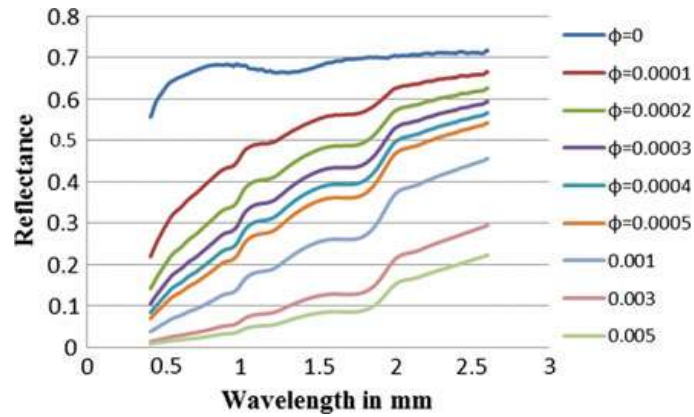


Fig. 3 Effect of iron fraction

3.2 Effect of Iron Fraction

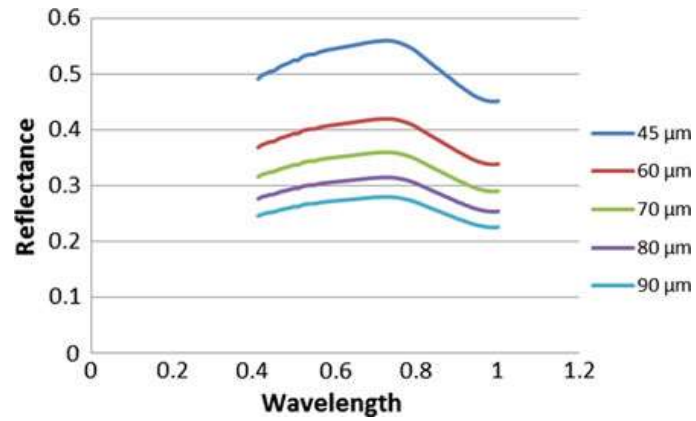
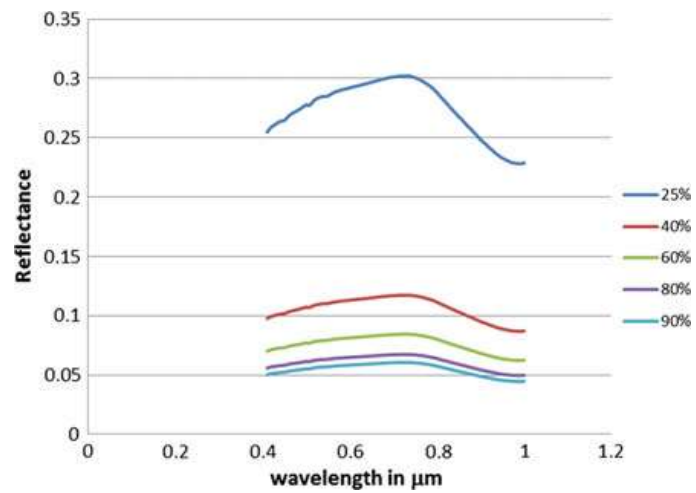
The sub-microscopic iron also termed as nano-phase iron is considered as a main product of space weathering. Long-time exposure to the lunar environment creates a thin layer of sub-microscopic iron which in turn influences on the lunar spectra. Figure 3 shows for the increasing value of iron leads to attenuation of the characteristic absorption, reddening of the slope continuum and the reduction in the overall reflectance. The degree of space weathering in the model is controlled by filling factor ϕ .

3.3 Effect of Grain Size

Grain size for the model is set to the laboratory specified upper and lower limits. However, the grain sizes cannot be generalized for all types of end members. Because some types of mineral like plagioclase can break easily will have finer grain size compared to other minerals. An average grain size was calculated for modeling. The overall reflectance increases with decreasing grain size due to the higher surface volume ratio and can be seen in Fig. 4.

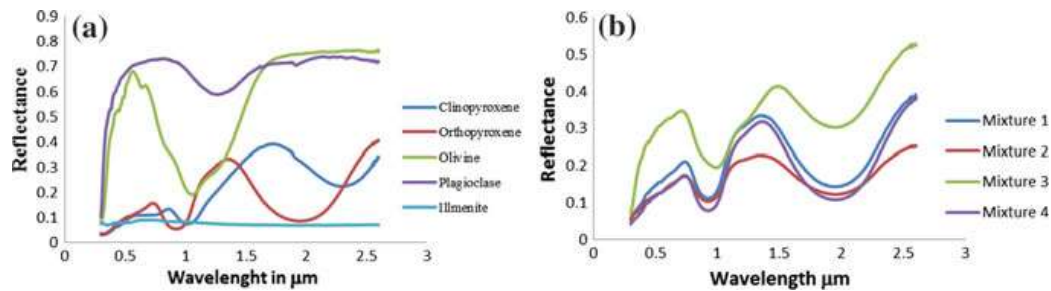
3.4 Effect of Porosity

The reflectance increases for denser material, whereas the reflectance significantly decreases for less denser materials. The porosity parameter k indirectly introduces the different values for the porosity within the model. The value for parameter K is connected through $P = 1 - \phi$, where P is the porosity, and the ϕ is the filling factor. For increasing filling factor, the porosity decreases, and for values much lower than 1, the porosity parameter becomes 1. Figure 5 shows the reflectance for different porosities.

Fig. 4 Effect of grain size**Fig. 5** Effect of porosity

4 Model Validation with Known Mixture Compositions

The final model is tested with the four standard lunar laboratory mixtures derived from the RELAB database and the testing result shows the good resemblance with the laboratory mixtures. The model is capable of reproducing the laboratory spectra. Figure 6 shows the end member spectra used for testing and the mixture spectra

**Fig. 6** a End member spectra. b Mixtures used for model evaluation

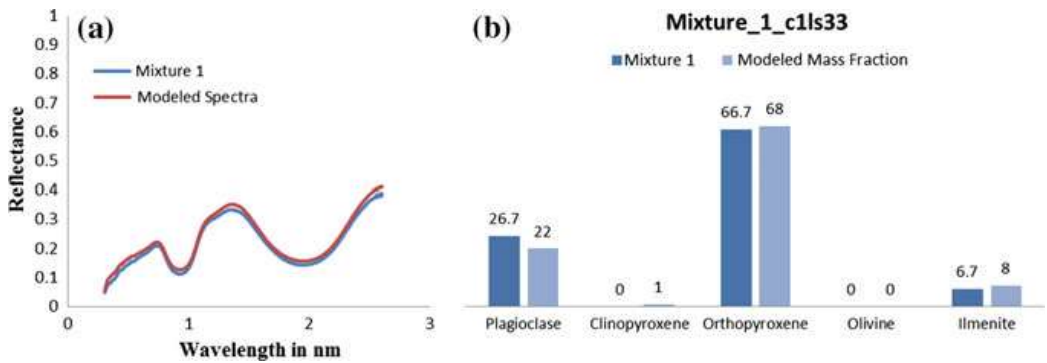


Fig. 7 a Measured and modeled spectra of mixture 1 with spectra id c1ls33 (Source RELAB).
b Difference of measured and modeled composition

for model evaluation. Figures 7, 8, 9, and 10 show the testing results along with the difference between actual measured compositions with modeled results. On an

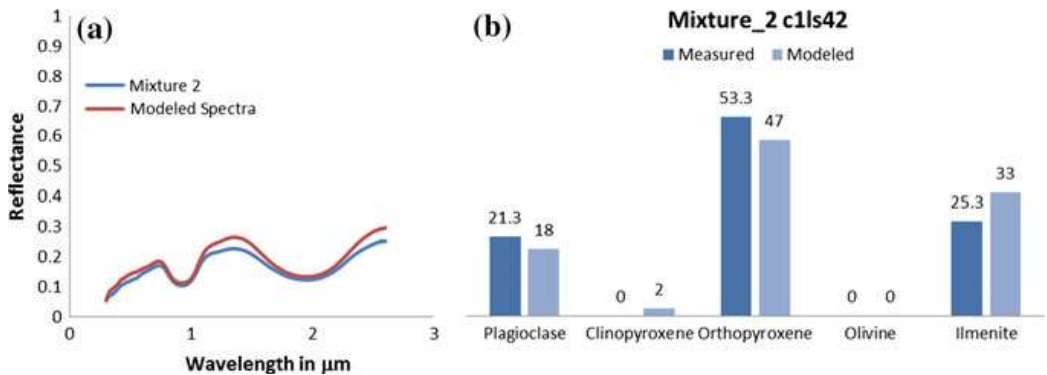


Fig. 8 a Measured and modeled spectra of mixture 2 with spectra id c1ls42 (Source RELAB).
b Difference of measured and modeled composition

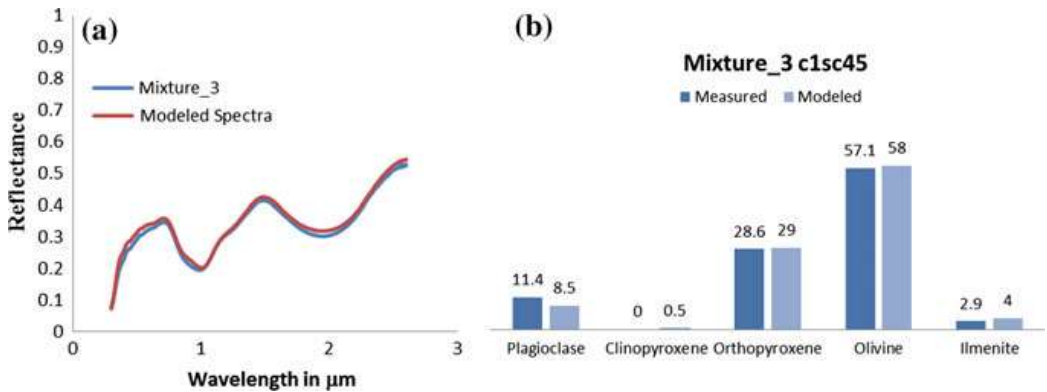


Fig. 9 a Measured and modeled spectra of mixture 3 with spectra id c1sc45 (Source RELAB).
b Difference of measured and modeled composition

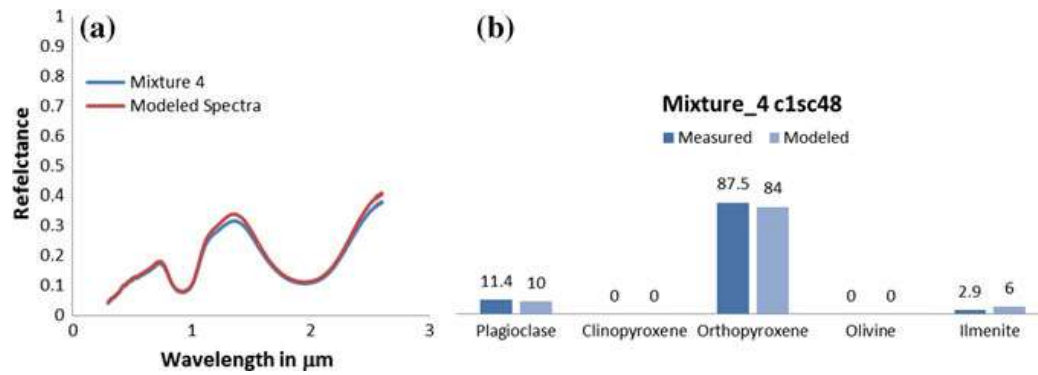


Fig. 10 a Measured and modeled spectra of mixture 4 with spectra id c1sc48 (Source RELAB).
b Difference of measured and modeled composition

average, 10% variation is observed within measured and modeled values and can be seen in the following figures.

4.1 Mixture 1

See Fig. 7.

4.2 Mixture 2

See Fig. 8.

4.3 Mixture 3

See Fig. 9.

4.4 Mixture 4

See Fig. 10.

5 Working with Chandrayaan-1 Hyperspectral Image from Mare Vaporum

The Mare Vaporum is located at the near side at southwest of mare serenitatis of the moon and centered at 13° N and 3° E. The diameter is around 230 km. The Mare Vaporum is also called as “sea of vapors,” and it was named by Mary A Blagg and K muller in 1935. The mare regions were classified by Hiesinger et al. [35] into six spectrally homogenous units. The image subset covering the study area from orbit number 1071 having product Id HYS_NREF_20090205T093223605 is shown in Fig. 11 where (a) shows the extent of the study area LROC wide-angle camera image and (b) shows the actual HySI coverage on the globe view software. Environment for visualizing images (ENVI 5.3) software was used for processing, analyzing, and deriving spectra from varying locations.

5.1 Image Preprocessing and Spectral Profile Extraction

The level-4 band to band registered HySI image downloaded from www.issdc.gov.in. The hyperspectral image consisting of 64 bands is in radiance format which is then converted to the apparent reflectance. The image is further cross calibrated with the 10,084 Apollo soil sample. The image is georeferenced using the coordinate information provided with the image itself. The image is further checked band by band for any type of noise and for any bad line or bad column which can be corrected by averaging with the adjacent line or column values.

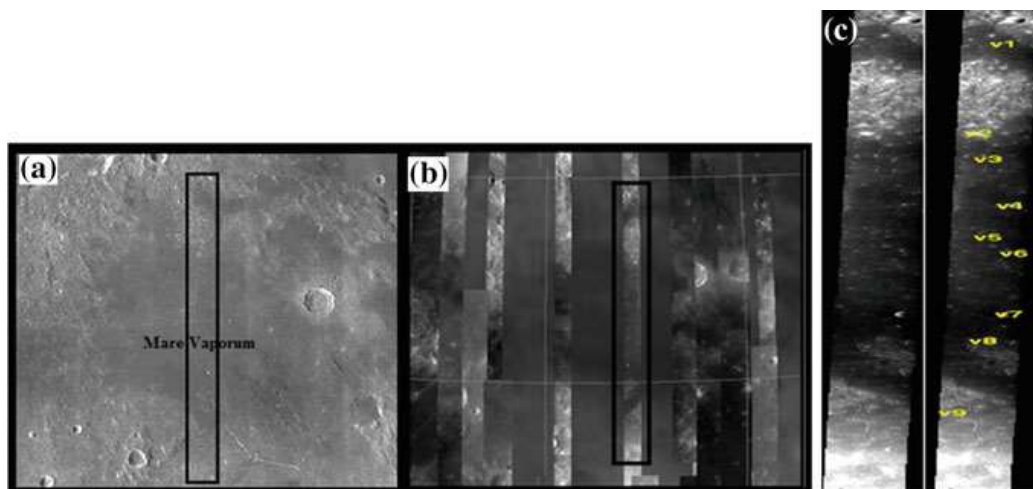


Fig. 11 HySI coverage shown on **a** LRO LROC WAC image **b** Globe view software from ISRO's ISSDC **c** The right image shows the original HySI dataset and left shows the sampling locations

6 Results and Discussion

The active spectra are shown in Fig. 12 which were selected by visual inspection from the fresh craters the spectra having strong slope, but no significant absorption trend is discarded or excluded from the further modeling process. The spectra having significant absorption trends are selected for modeling. However, the limited spectral coverage of the HySI sensor shows only the trend in the mineralogy, and because of HySI spectral range, we have clipped our selected model end members to HySI spectral range for final modeling. Each HySI spectra is interpolated using cubic spline interpolation function to match with the spectral resolution of pure end member which is 5 nm.

The active spectra collected from the very small fresh craters were spread across the mare area as the frequency is more for small craters and the iron volume fraction for such area are about 0.0001 showing the less mature areas. Spectra v1 and v8 showing more iron fraction values (0.00025) indicating relatively mature soil as it can be contaminated by highland materials and the percent of agglutinates is also around 35% for these spectra. The spectra showing absorption trends toward longer wavelengths exhibit 40% clinopyroxene and spectra v1, v5, and v8 having absorption around 900 nm and showing overall reduced reflection about 20% having 23–35% orthopyroxene. The mature surface having such absorption may be because the host soil may contain more iron. Table 1 shows the mass fraction of each mineral obtained from the model, and Table 2 represents the associated parameters obtained for corresponding spectra. The representative model and measured spectra can be seen in Fig. 13.

Fig. 12 Scaled reflectance spectra at 748.3 nm of Mare Crisium

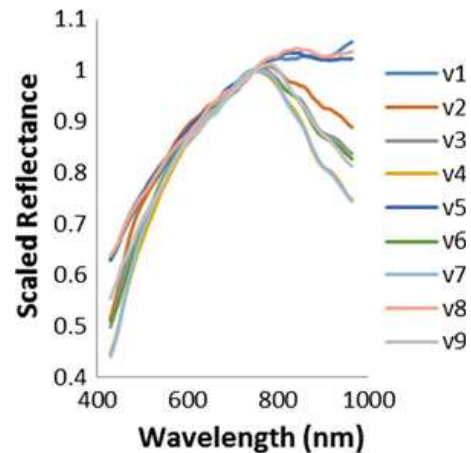
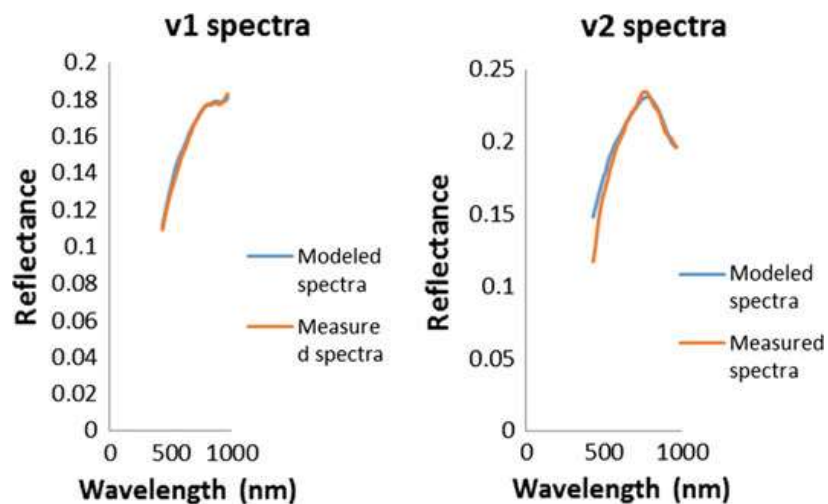


Table 1 Mineral mass fractions obtained from the modeling

Spectra Id	Plagioclase	Clinopyroxene	Orthopyroxene	Olivine	Agglutinates
v1	29	8	23	6	34
v2	33	38	8	7	14
v3	35	37	13	0	15
v4	36	37	10	2	15
v5	35	12	30	0	23
v6	30	39	15	0	16
v7	35	41	10	0	16
v8	36	2	36	0	26
v9	35	35	12	3	15

Table 2 Associated parameters for the corresponding modeled spectra

Spectra Id	Iron volume fraction	Average grain size	Porosity	Phase function	Rmse	Correlation coefficient
v1	0.00024	243	29	Average	0.001	0.9982
v2	0.0001	70	61	Average	0.002	0.993
v3	0.0001	72	60	Average	0.002	0.993
v4	0.0001	50	60	Average	0.002	0.9822
v5	0.00018	102	65	Average	0.0009	0.9985
v6	0.0001	103	55	Average	0.002	0.9846
v7	0.0001	58	55	Average	0.004	0.9774
v8	0.00026	79	60	Average	0.001	0.9972
v9	0.0001	73	58	Average	0.0003	0.9908

**Fig. 13** Sample measured and modeled spectra from Mare Vaporum

7 Conclusion

The radiative transfer model has been implemented for spectra derived from hyper-spectral images to model and quantify the lunar surface mineralogy. Parameter study is also conducted, and the influence and behavior of these parameters are in accordance with the model definitions. However, the grain size parameter cannot be generalized for all types of end members so an average grain size is considered during the modeling process. Spectra from the prominent bright areas are considered as they show significant absorption trend, but modeling the spectra from relatively matured areas which has undergone high degree of space weathering would be a challenge for modeling with the limited spectral coverage as of HySI. This issue can be addressed with data having wide spectral range and more number of end member can be employed for precise modeling of the spectra.

Acknowledgements “The author is thankful for the financial assistance received from DoS (Department of Space, ISRO/SSPO/Ch-1/2016-17, August 17, 2016). This work is a part of the ISRO project under Chandrayaan-1 AO (Announcement of Opportunity) program. The research is based (partially or to a significant extent) on the results obtained from the Chandrayaan-1, first lunar mission of the ISRO, archived at the Indian Space Science Data Center (ISSDC).”

References

1. Pieters, C.M., Fischer, E.M., Rode, O., Basu, A.: Optical effects of space weathering—the role of the finest fraction. *J. Geophys. Res.—Planets* **98**, 20817–20824 (1993)
2. Chapman, C.R.: Space weathering of asteroid surfaces. *Annu. Res. Earth Planet. Sci.* **32**, 539–567 (2004)
3. Keller, L.P., McKay, D.S.: Discovery of vapor deposits in the lunar regolith. *Science* **261**, 1305–1307 (1993)
4. Keller, L.P., McKay, D.S.: the nature and origin of rims on lunar soil grains. *Geochim. Cosmochim. Ac.* **61**, 2331–2341 (1997)
5. Taylor, L.A., Pieters, C.M., Keller, L.P., Morris, R.V., McKay, D.S.: Lunar Mare Soils: Space weathering and the major effects of surface-correlated nanophase Fe. *J. Geophys. Res. Planets* **106**, 27985–27999 (2001)
6. Taylor, L.A., Pieters, C.M., Patchen, A., Taylor, D.S., Morris, R.V., Keller, L.P., McKay, D.S.: Mineralogical and chemical characterization of lunar highland soils: Insights into the space weathering of soils on airless bodies, *J. Geophys. Res. Planets* **115**, E02002 (2010)
7. McCord, T.B., Johnson, T.V.: Lunar spectral reflectivity (0.30–2.50 microns) and implications for remote mineralogical analysis. *Science* **169**, 855–858 (1970)
8. McCord, T.B., Adam, J.B.: Progress in remote optical analysis of lunar surface composition. *Moon* **7**, 453–474 (1973)
9. Pieters, C.M., Taylor, L.A., Noble, S.K., Keller, L.P., Hapke, B., Morris, R.V., Allen, C.C., McKay, D.S., Wentworth, S.: Space weathering on airless bodies: resolving a mystery with lunar samples. *Meteorit. Planet. Sci.* **35**, 1101–1107 (2000)
10. Noble, S.K., Pieters, C.M., Keller, L.P.: An experimental approach to understanding the optical effects of space weathering. *Icarus* **192**, 629–642 (2007)
11. Hapke, B.: Effects of a simulated solar wind on the photometric properties of rocks and powders. *Ann. N. Y. Acad. Sci.* **123**, 711–721 (1965)

12. Hapke, B., Cohen, A., Cassidy, W., Wells, E.: Solar radiation effects on the optical properties of Apollo 11 lunar samples. In: Proceedings of the Apollo 11 Lunar Science Conference, pp. 2199–2212 (1970)
13. Nobel, S.K., Pieters, C.M.: Space weathering on mercury: implications for remote sensing. *Sol. Syst. Res.* **37**, 31–35 (2003)
14. Brunetto, R., Vernazza, P., Marchi, S., Birlan, M., Fulchignoni, M., Orofino, V., Strazzulla, G.: modeling asteroid surfaces from observations and irradiation experiments: the case of 832 Karin. *Icarus* **184**, 327–337 (2006)
15. Shkuratov, Y.G., Starukhina, L., Huffmann, H., Arnold, G.: A model of spectral albedo of particulate surfaces: Implications for optical properties of the moon. *Icarus* **137**(2), 235–246 (1999). <https://doi.org/10.1006/icar.1998.6035>
16. Hapke, B.: Bidirectional reflectance spectroscopy. I—Theory. *J. Geophys. Res.* **86**, 3039–3054 (1981)
17. Sunshine, J.M., Pieters, C.M., Prait, S.F.: Deconvolution of mineral absorption bands: an improved approach. *J. Geophys. Res.* **95**(B5), 6955–6966 (1990). <https://doi.org/10.1029/JB095iB05p06955>
18. Poulet, F., Erard, E.: Nonlinear spectral mixing: quantitative analysis of laboratory mineral mixtures. *J. Geophys. Res.* **109**, E02009 (2004). <https://doi.org/10.1029/2003JE002179>
19. Hapke, B., Wells, E.: Bidirectional reflectance spectroscopy. II experiments and observations. *J. Geophys. Res.* **86**, 3055–3060 (1981)
20. Hapke, B.: Bidirectional reflectance spectroscopy. III-Correct. Macrosc., *Icarus* **59**, 41–59 (1984)
21. Hapke, B.: Bidirectional reflectance spectroscopy. IV-the extinction coefficient and the opposition effect. *Icarus* **67**, 264–280 (1986)
22. Hapke, B.: Theory of Reflectance and Emittance Spectroscopy, Topics in Remote Sensing, Cambridge University Press, Cambridge, UK (1993)
23. Hapke, B.: Space weathering from mercury to the asteroid belt. *J. Geophys. Res.* **106**, 10039–10074 (2001)
24. Clark, R.N., Roush, T.L.: Reflectance spectroscopy: quantitative analysis techniques for remote sensing applications. *J. Geophys. Res.* **89**, 6329–6340 (1984). <https://doi.org/10.1029/JB089iB07p06329>
25. Mustard, J.F., Pieters, C.M.: Quantitative abundance estimates from bidirectional reflectance-measurements. Proc. Lunar Planet. Sci. Conf. 17th, Part 2 *J. Geophys. Res.* **92**, E617–E626 (1987). <https://doi.org/10.1029/JB092iB04p0E617>
26. Lucey, P.G.: mineral maps of the moon. *Geophys. Res. Lett.* **31**, L08701 (2004). <https://doi.org/10.1029/2003GL019406>
27. Lawrence, S.J., Lucey, P.G.: Radiative transfer mixing models of meteoritic assemblages. *J. Geophys. Res.* **112**, E07005 (2007). <https://doi.org/10.1029/2006JE002765>
28. Cahill, J.T.S., Lucey, P.G., Wiecek, M.A.: Compositional variations of the lunar crust: results from radiative transfer modeling of central peak spectra. *J. Geophys. Res.* **114**, E09001 (2009). <https://doi.org/10.1029/2008JE003282>
29. Cahill, J.T.S., Lucey, P.G., Stockstill-Cahill, K.R., Hawke, B.R.: Radiative transfer modeling of near-infrared reflectance of lunar highland and mare soils. *J. Geophys. Res.* **115**, E12013 (2010). <https://doi.org/10.1029/2009JE003500>
30. Hiroi, T., Pieters, C. M.: Estimation of grain sizes and mixing ratios of fine powder mixtures of common geologic minerals. *J. Geophys. Res.* **99**, 10867–10880 (1994)
31. Kitamura, R., Pilon, L., Jonasz, M.: Optical constants of silica glass from extreme ultraviolet to far infrared at near room temperature. *Appl. Opt.* **46**, 8118 (2007)
32. Johnson, P.B., Cristy, R.W.: Optical constants of metals: Ti, V, Cr, Mn, Fe, Co, Ni, and Pd, prb, **9**, 5056–5070 (1974)
33. Mustard, J.F., Pieters, C.M.: Photometric phase functions of common geologic minerals and applications to quantitative analysis of mineral mixture reflectance spectra. *J. Geophys. Res.* **94**, 13619–13634 (1989)

34. Hapke, B.: Bidirectional reflectance Spectroscopy5. Coherent Backscatter Oppos. Eff. Anisotropic Scatt., *Icarus* **157**, 523–534 (2002)
35. Hiesinger, H., Head III, J.W., Wolf, U., Jaumann, R., Neukum, G.: Ages and stratigraphy of mare basalts in oceanus procellarum, mare nubium, mare cognitum, and mare insularum. *J. Geophys. Res.: Planets* **108**(E7) (2003)